ELSEVIER

Colloids and Surfaces
A: Physicochemical and Engineering Aspects 118 (1996) 263–272

COLLOIDS AND SURFACES A

The influence of surface films on near-surface vortical flows

Sean P. McKenna *, Wade R. McGillis, Erik J. Bock

Department of Applied Ocean Physics and Engineering, Woods Hole Oceanographic Institution, Woods Hole, MA 02543, USA

Received 10 February 1996; accepted 21 February 1996

Abstract

An experimental apparatus was designed and constructed to generate reproducible vortex rings in the laboratory. These rings were produced in a small test tank and were allowed to propagate upward where they then interacted with an air/water interface. Tests were performed on the following surfaces: a clean free distilled water surface, a solid polycarbonate wall, and the surface of a 1 μm solution of Triton X-100 in distilled water. The vortex rings studied in the present investigation ranged in Froude number from 0.042 to 0.164 and in Reynolds number from 1772 to 6785. Measurements of the two-dimensional near-surface flow field were made using the technique of particle image velocimetry (PIV). Preliminary results show, (i) that the experimental set-up employed in this study is able to generate repeatable vortex rings with varying strengths and propagation speeds, (ii) that the PIV system used to quantify the experimental observations is capable of resolving spatial velocity fields of the flow accurately, and (iii) that the presence of the surface active film studied here profoundly affects the dynamics of the interaction between the vortex rings and the surface of the solution. These effects were observed to manifest themselves in several ways which included vortex path modification, production of secondary and tertiary vortices, and a measured impact on total circulation and vorticity.

Keywords: Air/water interface; Near-surface; Particle image velocimetry; Viscoelasticity; Vortex ring

1. Introduction

There has been a significant amount of computational and experimental work done on the topic of a vortex pair (two counter-rotating vortices of equal strength) interacting with a free surface. The motivation for these studies has been varied. Barker and Crow [1] investigated the interaction of a pair of line vortices with a solid boundary and a free surface in an effort to learn more about the trailing vortex pair that is shed from aircraft wings. Sarpkaya and Henderson [2] studied the surface deformations resulting from the free surface interaction of a trailing vortex pair that was generated by towing a submerged delta wing at a negative angle of attack. Their particular interest was to better understand the surface signature of ship wakes with direct application to remote sensing (see also Tsai and Yue [3]). More recently, studies have focused on near-surface turbulence and its role in gas and heat exchange across the air/sea interface (Ohring and Lugt [4]; Tryggvason et al. [5]; Hirsa and Willmarth [6]). These few examples demonstrate the diverse history of this subject. A more thorough summary of the literature on the subject of vortex rings and pairs was given by Tryggvason et al.

The importance of surfactants on vortex–surface interaction was shown when Bernal et al. [7]

* Corresponding author.

PII S0927-7757(96)03691-6

discovered that the degree of surface contamination had a direct impact on the dynamics of the vortex pair at the surface. Specifically, they observed that the vortex pair rebounded away from even a slightly contaminated surface. Interestingly, it should be noted that this observation of rebounding was actually first reported by Barker and Crow, but they failed to provide a sound explanation for its occurrence. Bernal et al. also noted the formation of secondary and tertiary vortices as a result of surface contamination. They found that both the rebounding effect and the ancillary vortex formation were reduced when a cleaner surface was tested. They concluded that the presence of a surface film generates secondary vorticity as the vortex pair reaches the surface, and inhibits the outward motion of the primary vortex.

With this realization of the effects of the surface condition on vortical motion at the surface, more recent studies have been conducted in an effort to quantify these phenomena. The experimental work of Hirsa and Willmarth that was complemented by the numerical analysis of Tryggvason et al. is closely related to the present study of a vortex ring impinging on a free surface. Hirsa and Willmarth presented their observations of the surface features and their measurements of the subsurface flow field (using the particle image velocimetry (PIV) technique) that result from the interaction of a vortex pair with a free surface. Their study reported experiments performed using both a clean surface and a known surfactant (oleyl alcohol). Both the experimental work of Hirsa and Willmarth and the theoretical modeling of Tryggvason et al. showed that the presence of surface contamination results in the production of secondary, opposite-signed vorticity outboard of the primary vortices which causes the primary vortices to rebound from the surface in a similar fashion to a vortex pair colliding with a solid wall (no-slip boundary).

As was briefly mentioned earlier, the study of vortical flows interacting with a free surface is now being applied to the topic of near-surface turbulence. Gaining a better understanding of the processes involved with near-surface turbulence is important because it directly relates to air–sea interaction phenomena. The transfer of gas and heat across the air–sea boundary is influenced by many factors, one of which is the degree and nature of the turbulence/mixing in the uppermost layers of the ocean. To what degree this mixing enhances the transfer rate of these quantities is a current topic of interest. The dynamics of near-surface mixing is, in turn, affected by a number of different hydrodynamic mechanisms. One of the more dominant subsurface mechanisms is the interaction of coherent vortical flows with the free surface. Thus, the investigation of vortex pairs and rings colliding with a free surface is intended to aid in the understanding of near-surface turbulence and transport phenomena. The underlying reasoning behind the selection of vortex pairs and rings for study is that they provide a well-defined fluid dynamic structure that can be relatively easily generated in the laboratory as well as simulated numerically.

In this study, experiments were performed with vortex rings of varying strength and propagation velocity. The surface boundary conditions studied included a clean free surface, a solid wall boundary, and a free surface with a surfactant. The solid wall condition was chosen to provide a point for comparison.

Previous experimental work in this area has often used the rather vague terms, 'contaminated' and 'cleaner', to qualify the condition of the surface. In the case of Bernal et al. for example, the water used in their experiments was qualified as being tap water that had been left uncovered for two weeks. Improvements were made by Hirsa and Willmarth who introduced a known concentration of surfactant into their experimental water. The work presented here characterizes the surfactant concentration, which is an important step in fully understanding the role of surface films in near-surface interaction dynamics.

2. Experimental techniques

Research was done on vortex ring generators, and several different designs were found in the literature. In a very mechanical set-up, Maxworthy [8] employed a cam and follower arrangement that drove a horizontally mounted piston inside a variable cross-section nozzle. The effect of this apparatus was to eject a slug of fluid from the

nozzle where it then rolled up into a vortex ring and proceeded downstream through a glass test tank. Another piston driven vortex generator was utilized by Willert and Gharib [9]. A vertically oriented vortex ring generator was employed by Glezer and Coles [10] in their turbulent ring experiments. In their design, an annular-outlet solenoid valve was used to control the flow of a pressurized water supply. Downstream of the solenoid valve was a lightweight piston located in a cylindrical chamber which discharged into the visualization tank. This system was arranged such that the vortex rings were ejected downward into the tank. The actual generation of the rings was accomplished by opening the solenoid valve for a fraction of a second, allowing a small slug of fluid to be forced against the piston which then pushed the fluid in the cylindrical chamber out the nozzle where roll-up took place.

A vortex ring generator similar to the one used by Bernal et al. was used in these experiments. Fig. 1 illustrates the square test tank (20.3 cm inner dimensions) fabricated from five square glass segments bonded together with commercially available aquarium sealant. The bottom segment contained an opening in its center that allowed the vortex tube to pass through it. Throughout all of the experiments, the water line was held at a constant height 10.5 cm from the mouth of the vortex tube. This was accomplished by positioning a surface drain tube at the desired height. This tube was connected to a low power pump which perpetually drew water from the surface. This had two beneficial effects. First, it maintained a constant water level (and constant hydrostatic head) during the course of the experiments which was necessary since the vortex generator introduced a small amount of fluid into the tank each time it was operated. Second, it served the function of continually aspirating the surface, keeping it free from any airborne deposits or contamination.

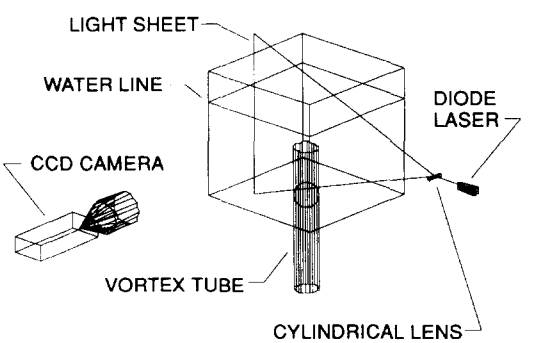

Fig. 1. Particle image velocimetry components and arrangement.

Vortex rings were produced when a solenoid valve was triggered open for a fraction of a second. Due to the system being under constant pressure, this action results in a small slug of fluid being forced through the system and out the pipe where the fluid rolls up into a ring. This ring then convects upward toward the surface.

The technique of particle image velocimetry (PIV) was used in order to extract both qualitative and quantitative information about the two-dimensional subsurface flow field generated by the interaction of a vortex ring with a free or solid surface. This technique provides a non-invasive, spatially intensive velocity measurement at a single instant in time. Hence, PIV is quite different from the more traditional methods of measuring fluid flow velocities such as hot wire or film anemometry since these techniques inherently perturb the flow and provide velocity measurements at only a single point.

In the PIV technique, two sequential, single-exposed video fields are extracted from recorded camera video, digitized, and then analyzed computationally through a local spatial cross-correlation algorithm. Fig. 1 shows the components of the PIV system. Not shown in this figure is the fact that the water in the test tank is seeded with microscopic particles that follow the fluid motion. In these experiments, two types of particles were used separately: aluminum oxide particles (1–5 μm), and polystyrene spheres ($\approx$50 μm). The aluminum oxide was selected due to its favorably high index of refraction. However, its specific gravity was such that these particles would settle out of the fluid in time. However, the polystyrene spheres had a specific gravity close to that of water and thus remained neutrally buoyant in the fluid, but they possessed a relatively lower index of refraction. Satisfactory cross-correlation results were obtained using both types of seed particles with varying seeding densities. Excellent flow visualization was

achieved with a large seeding density of aluminum oxide particles.

A Pulnix TM7-EX CCD camera was positioned with a line of sight that was perpendicular to one of the tank walls. A 30 mW laser diode was used to produce a beam of light (wavelength, 690 nm) which is then transformed into a 1 mm thick, two-dimensional light sheet by passing it through a cylindrical lens. This light sheet is oriented through the axis of the pipe and orthogonal to the camera line of sight. With all of the experiments conducted under dark conditions, the effect of the light sheet is to illuminate only the seed particles that are present in the two-dimensional plane directly above the vortex generator. Thus, when a vortex ring propagates upward from the pipe and the laser is activated, the camera sees only the illuminated particles thereby capturing a cross-sectional view of this three-dimensional structure.

The video output of the camera was recorded using a BVW-75 BETACAM SP recorder. This method was very useful since by producing a video recording of each run, continuous temporal data could be extracted. Once a complete data set had been acquired, the BETACAM recording of each run was then interrogated field by field. Temporal identification and consistency were maintained by using the LED time stamp. Selected pairs of sequential fields were digitized and written to a 1 GB optical disk on a DECstation 5000.

The PIV method relies on using two digital images to ascertain the displacement of particles between video fields. Then, by invoking the time separation between fields, velocities can be determined. The term 'particle pairs' is often used to describe a particle in one image and its partner (actually itself, only displaced) in the subsequent image. The task of determining particle pairs and displacements is accomplished by performing local spatial cross-correlations on each image pair (image 1 and image 2). The cross-correlation coefficient for one combination of local images is expressed as

$$C_{i,j} = \frac{\sum_{k=x_0}^{k=x_n}\sum_{l=y_0}^{l=y_n}[(f_{k,l}-\bar{f})(g_{k+i,l+j}-\overline{g_{i,j}})]}{\sqrt{\sum_{k=x_0}^{k=x_n}\sum_{l=y_0}^{l=y_n}(f_{k,l}-\bar{f})^2}\sqrt{\sum_{k=x_0}^{k=x_n}\sum_{l=y_0}^{l=y_n}(g_{k+i,l+j}-\overline{g_{i,j}})^2}}$$

where x_0 and y_0 denote the lower-left corner of the square interrogation window of size $n+1$; $\bar{f}$ and $\overline{g_{i,j}}$ are defined as:

$$\bar{f} = \frac{\sum_{k=x_0}^{k=x_n}\sum_{l=y_0}^{l=y_n} f_{k,l}}{(n+1)^2}$$

and

$$\overline{g_{i,j}} = \frac{\sum_{\alpha=x_0+i}^{\alpha=x_n+i}\sum_{\beta=y_0+j}^{\beta=y_n+j} g_{\alpha,\beta}}{(n+1)^2}$$

In these three expressions, all indices denote pixel coordinates. $f_{k,l}$ represents the matrix of pixel values for the interrogation window in image 1. $g_{k+i,l+j}$ represents its partner matrix of pixel values for the search window in image 2. As can be seen from the numerator of this equation, both $f_{k,l}$ and $g_{k+i,l+j}$ are thresholded from the mean pixel intensities, f and $g_{i,j}$, of each local image respectively. Each of the two components of the denominator is the square root of the sum of the variances for each pixel location. Division by the product of these two quantities has the effect of normalizing the numerator value. The value $C_{i,j}$ ranges from -1 to 1, with 1 signifying complete positive correlation (-1 indicates complete negative correlation, and a value of 0 results when the two images are uncorrelated). All negative values are discarded and are assigned a correlation of 0. An entire two-dimensional array of coefficents is then produced by shifting the search window horizontally and vertically one pixel at a time and computing the correlation at each new location.

The results from the statistically intensive computations were a large correlation peak in space centered about the position where the center of the interrogation window of particles in image 1 has moved to in image 2. Other smaller peaks may be observed, and these are the result of either particle pair mismatch and/or particles entering or leaving the interrogation windows. At this stage, a three-point gaussian curve fit is applied to the primary correlation peak in both the x and y directions. The x and y coordinates of the intersection of the two curves mark the point of displacement for the particles in the interrogation

window of image 1. The coordinates of this point are measured to sub-pixel accuracy. The distance that is translated therefore represents the average particle displacement for that particular region. A velocity vector is drawn from the center of the original interrogation window to the point of displacement, and the entire procedure is repeated for all of the interrogation regions in image 1 resulting in a two-dimensional velocity vector map of the flow field captured by the camera. Directional ambiguity is not a problem since this technique uses two separate images whose temporal positions are readily known. Enhanced computational resolution can be achieved by overlapping the interrogation regions.

At the start of each segment of experimentation, the complete vortex generation system was thoroughly cleansed. This involved disassembling the apparatus and washing each component with a laboratory-grade liquid detergent. Once this was done care was taken when handling the elements. Each part was then heavily rinsed with deionized, distilled water and then reassembled. A stainless steel container was filled with distilled water and pressurized. In the case where the effects of a surface film were to be analyzed, Triton X-100, a non-ionic surfactant, was used. A one micromolar solution was made, the steel container was filled with this solution, and the system was filled. To simulate the collision of a vortex ring with a solid

Table 1
Vortex parameters

Vortex ring	δ (cm)	Γ_{est} (cm^2 s^{-1})	Re	Fr
1	5.77	18.2	1772	0.042
2	5.58	26.8	2609	0.065
3	5.38	46.7	4546	0.119
4	5.69	69.7	6785	0.164

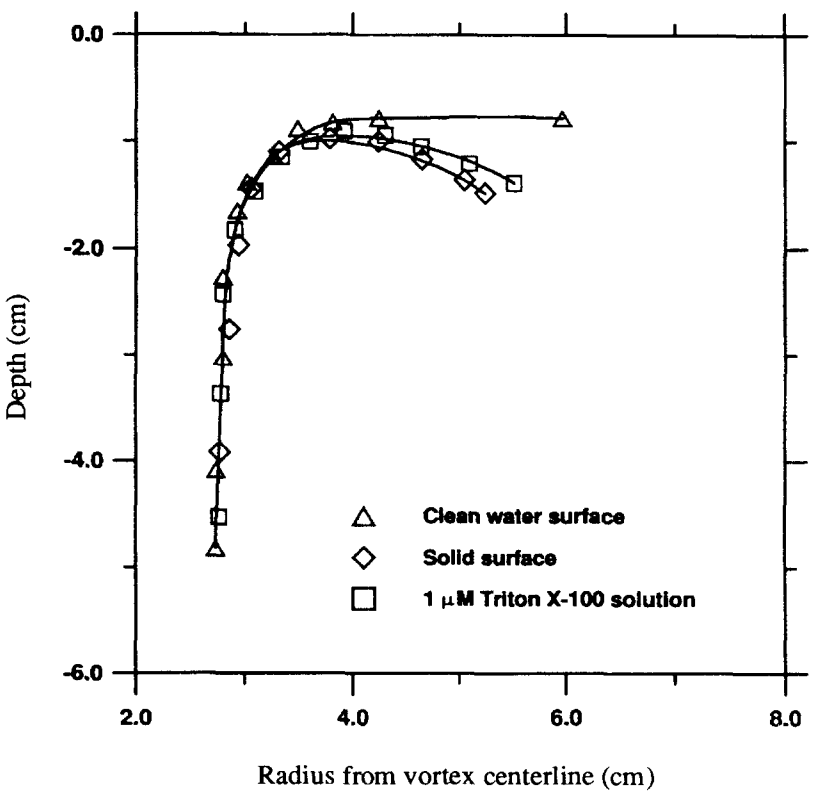

Fig. 2. Trajectories of vortex center below air/water interface.

surface, a square piece of polycarbonate (17.8 cm on a side) was rigidly suspended horizontally in the tank just below the water line.

Vortex rings of varying strength and propagation velocity were generated by controlling both the system pressure and the length of time the solenoid valve was open. The pertinent fluid dynamic parameters corresponding to these four rings are summarized below in Table 1.

The estimated circulation for each ring, Γ_{est}, was computed from the expression, $\Gamma_{est} = 0.5U^2\Delta t$, where U is the piston velocity and t is the time for which the solenoid is open. This expression results from balancing the momentum flux imparted to the fluid in the pipe with the fluid convection that ensues. Since the Froude numbers for these vortex rings were small, the surface was deformed very little when interaction took place. Several runs were performed for each ring at each surface condition.

3. Results and discussion

Using the BETACAM video recordings of the experiments, evolutions of the path tracked by the primary vortex core were generated in two dimensions. Analysis was performed for vortex rings 1, 3, and 4, and for all surface conditions. This involved manually locating the apparent center of the right-hand vortex core on a projected screen image of the video at various temporal positions during each evolution. (Willmarth et al. [11] discuss a similar procedure.) Fig. 2 shows the results of plotting vortex core positions beginning at an arbitrary time after initial roll-up. On all plots, the line $y = 0$ corresponds to the interface, and the line $x = 0$ represents the axis of the vortex ring. This plot is in agreement with what has been reported in the previous literature [6,7,12]. Consistent with what theory predicts for a stress-free, full-slip

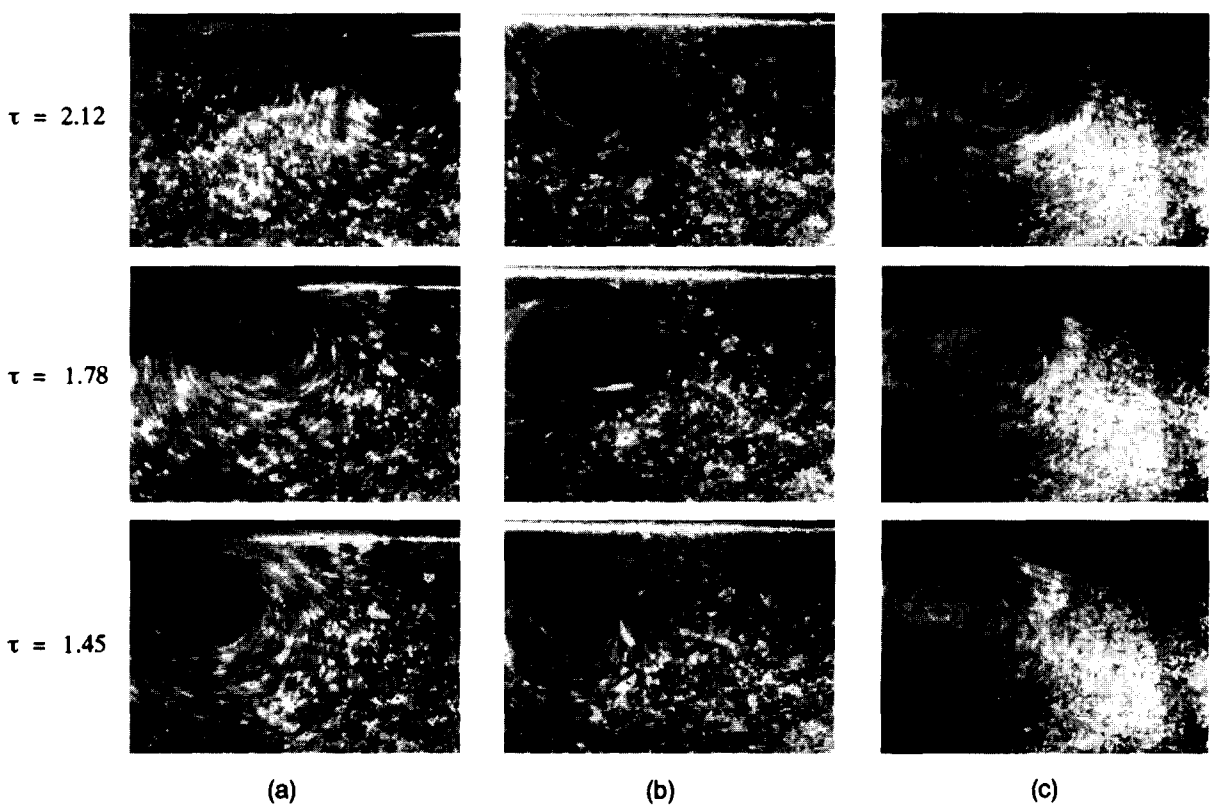

Fig. 3. Flow visualization of the evolution of subsurface vortex ring for (a) clean water surface; (b) a solid surface; (c) a 1 μm Triton X-100 solution at three different times.

boundary, the vortex core moves parallel to the water line upon interaction with a clean surface, increasing the ring diameter. Easily seen is the rebounding effect for both the solid surface and the Triton X-100 solution. Thus, it seems as if Triton X-100 has an effect intermediate between a full-slip and a no-slip boundary. This effect is similar to that predicted by Levich [13] for propagating waves in the presence of finite surface dilational viscoelasticity. We intend to pursue a more quantitative measure of surface dilational viscoelasticity in future studies.

Using a high seeding density of aluminum oxide particles and continuous laser illumination, excellent flow visualization of vortex ring evolutions was achieved. In order to compare vortex rings of varying propagation speeds, a dimensionless time, τ, thoughtfully defined by Hirsa and Willmarth, was used. This parameter is defined as

$$\tau = \frac{t - t_1}{\delta / U_p}$$

where t is the time since the solenoid was closed (start of vortex evolution), t_1 is the time elapsed from when the solenoid was closed until the ring reaches a depth equal to δ, and U_p is the ring propagation speed before interaction with the surface. Fig. 3 shows a typical vortex ring convecting toward three different surfaces. In this figure, a series of close-up flow visualization images for the right-hand vortex at increasing values of τ is shown. The field of view is approximately 3 cm × 2 cm. For the clean surface, the vortex propagates outward, parallel to the water line; its core diameter is reduced due to viscous dissipation effects. For the solid wall case, secondary and tertiary vortices were formed. Also shown in Fig. 3 is a similar series for the Triton X-100 solution. A secondary vortex with opposite rotation can be easily seen spinning off the primary vortex. Qualitatively, these images illustrate the significant effect surface films have on near-surface vortical flows. The similarity between the surfactant cases with the solid wall case is striking, and supports the idea that these films act like a quasi-solid boundary at the free surface.

Presented in Fig. 4 is a sample image of illuminated seed particles and the resulting velocity vector map that was generated by the PIV algorithm. This particular instance is for the Triton X-100 solution for $Re = 1772$. The uppermost row of vectors should be disregarded since it corresponds to the correlation of the total internal reflection of the flow beneath the surface. This vector map is in excellent agreement with the fluid motion seen in the video image. Velocity vectors could be computed for the high vorticity region in the core. This is a marked improvement on the PIV results reported by Hirsa and Willmarth. Also of significance is the fact that the vector map reveals the secondary, and even tertiary, vortices being produced as a result of surface interaction.

In order to quantify the effects of surface interactions on vortex flow, vorticity maps are generated using the local velocity gradients. In cylindrical coordinates, the local azimuthal vorticity is given as:

$$\omega_\phi = \frac{\partial u}{\partial z} - \frac{\partial w}{\partial r}$$

The vorticity fields computed from our experimental observations for a solid and free surface at the same time in the vortex evolution are shown in Fig. 5. The lightest intensity represents the largest positive vorticity and the darkest intensity represents the largest negative vorticity. For the clean, free surface no negative vorticity was generated. There are two negatively signed vortices present in the solid surface case.

A measure of the total amount of vorticity for each vector map was numerically computed. Batchelor [14] suggested that a measure of the total amount of vorticity in an area can be obtained from the quantity, $\bar{\omega} = 0.5 \int \omega^2 \, dA$. A plot of $\bar{\omega}$ vs. τ for three different surface conditions at $Re = 2609$ is shown in Fig. 6. The clean surface shows a dissipation due to viscous effects. However, the total vorticity in the solid wall and surfactant cases shows a greater decrease due to shear interactions of the vortex and the interface. At a τ of approximately 1, the effects of the surface viscoelasticity induced by the Triton solution can be seen. Again, the surfactant acts similarly to the solid wall boundary. There was not substantial

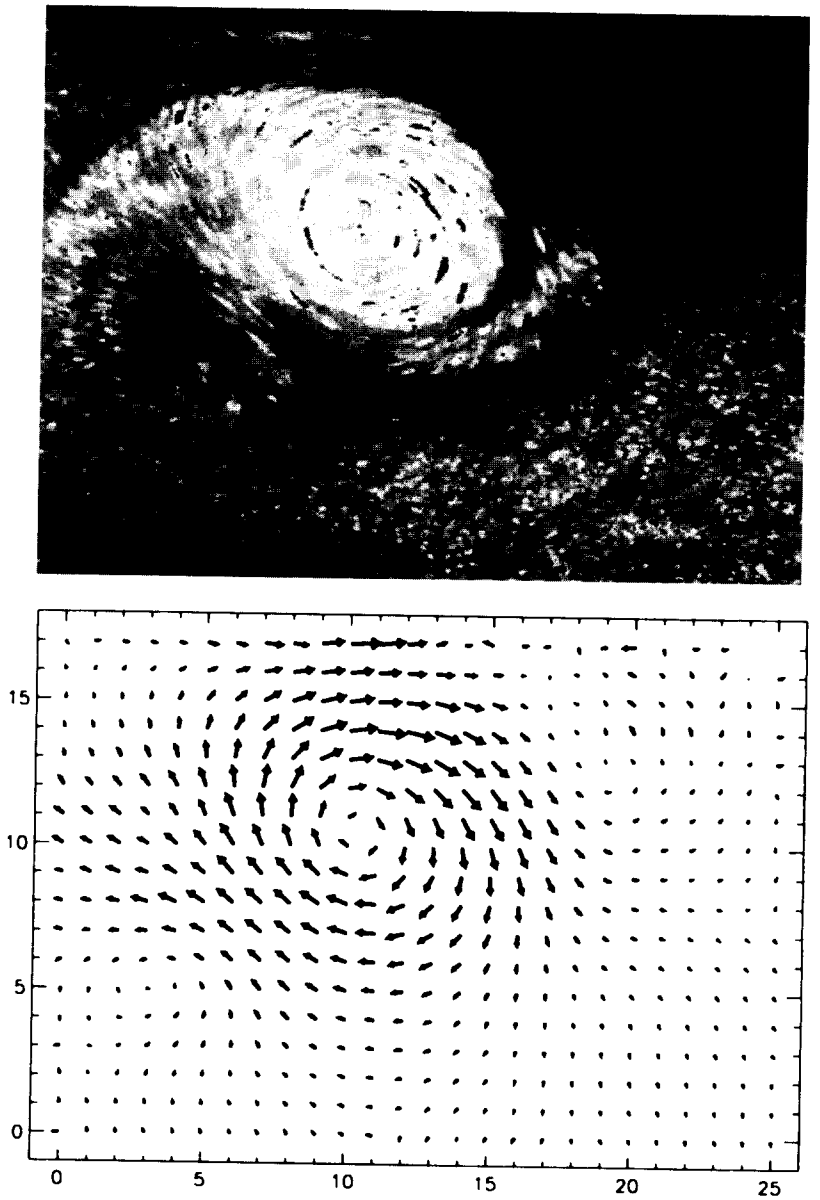

Fig. 4. Digitized image and calculated velocity field of vortices during interaction with the interface in a 1 μm Triton X-100 solution. Primary, secondary, and tertiary vortices are produced.

dissipation for the clean case for this range of τ values. A crucial feature of this plot is that each data point is the result of moving the camera to a location that completely encompasses the primary vortex structure. Therefore, this plot should indicate valid trends in the vortex circulation over time.

4. Conclusions

The modification of a vortical flow structure by a contaminated free surface has only recently become a popular topic of interest, and it has currently prompted several studies on this subject. The present study has provided innovative quanti-

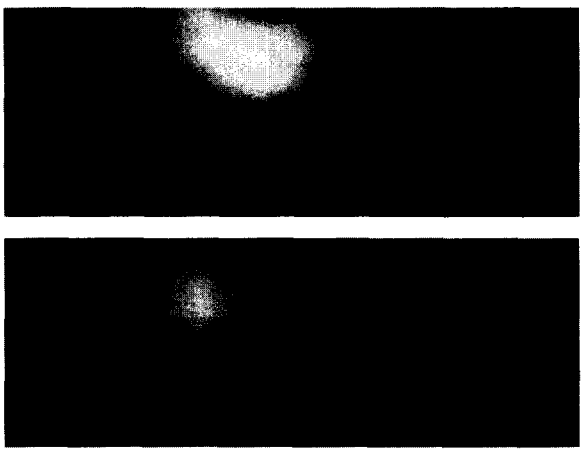

Fig. 5. Vorticity fields (ω_ϕ) for a vortex interaction with a clean surface (top) and a solid surface (bottom). Both images represent data taken at the same time delay after vortex generation.

tative results from a series of laboratory experiments on vortex rings interacting with a variety of free surfaces. This has contributed significantly to a better understanding of the role of surfactants on these fluid structures.

Consistent with the previous investigations, a rebounding effect was observed for surfaces with a surfactant present. In addition to this rebound, there existed a critical diameter at which the vortex ring ceased expanding and became chaotic. Using digital particle image velocimetry, velocity vector maps were generated that enabled the computation of a total vorticity for each vector map domain. As interaction takes place, viscous effects begin to dissipate the vortex circulation. Secondary and tertiary vortices are shed as the boundary layer near the surface breaks down. Eventually, the flow becomes chaotic and three-dimensional. It is apparent from the results presented here that a contaminated free surface can be considered to act very similarly to a solid wall boundary.

Acknowledgments

This work was supported by the National Science Foundation under Grant OCE-9301334

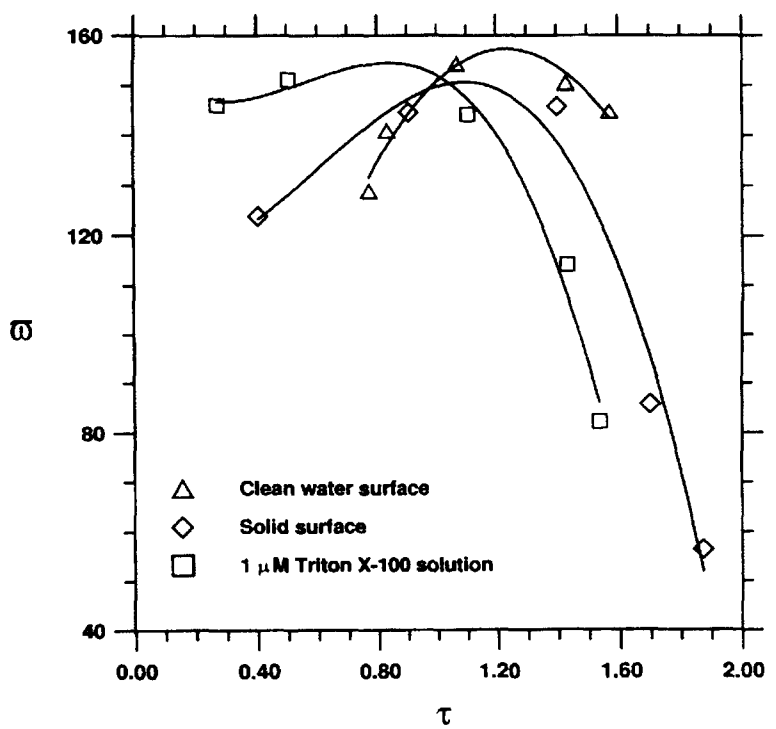

Fig. 6. Evolution of total vorticity for vortex–surface interaction.

and the Woods Hole Oceanographic Institution (contribution No. 9127).

References

[1] S.J. Barker and S.C. Crow, J. Fluid Mech., 82 (1977) 659.
[2] T. Sarpkaya and D.O. Henderson, AIAA Report No. 85-0445 (1985).
[3] W. Tsai and D.K.P. Yue, J. Fluid Mech., 289 (1995) 315.
[4] S. Ohring and H.J. Lugt, J. Fluid Mech., 227 (1991) 47.
[5] G. Tryggvason, J. Abdollahi-Alibeik, W.W. Willmarth and A. Hirsa, Phys. Fluids, A4 (1992) 1215.
[6] A. Hirsa and W.W. Willmarth, J. Fluid Mech., 259 (1994) 25.
[7] L.P. Bernal, A. Hirsa, J.T. Kwon and W.W. Willmarth, Phys. Fluids, A1 (1989) 2001.
[8] T. Maxworthy, J. Fluid Mech., 81 (1977) 465.
[9] C.E. Willert and M. Gharib, Experiments Fluids, 10 (1991) 181.
[10] A. Glezer and D. Coles, J. Fluid Mech., 211 (1990) 243.
[11] W.W. Willmarth, G. Tryggvason, A. Hirsa and D. Yu, Phys. Fluids, A1 (1989) 170.
[12] J.D.A. Walker, C.R. Smith, A.W. Cerra and T.L. Doligalski, J. Fluid Mech., 181 (1987) 99.
[13] V.G. Levich, Physicochemical Hydrodynamics, Prentice Hall, 1962, p. 610.
[14] G.K. Batchelor, An Introduction to Fluid Dynamics, Cambridge University Press, 1967, pp. 266–273.